Microstructure and magnetic properties of the Cu-rich Nd(Fe,Mo)_12 strip cast flakes

Sorana Luca, Johann Fischbacher, Camille Flament, Ryan Sedek, Patricia de Rango, Gabriel Gomez Eslava, Thomas Schrefl

Journal of Alloys and Compounds 1010 (2025) 178039

Contents lists available at ScienceDirect

Journal of Alloys and Compounds

journal homepage: www.elsevier.com/locate/jalcom

Microstructure and magnetic properties of the Cu-rich $Nd(Fe,Mo)_{12}$ strip cast flakes

Sorana Luca [a,*], Johann Fischbacher [b], Camille Flament [a], Ryan Sedek [a,c], Patricia de Rango [c], Gabriel Gomez Eslava [a], Thomas Schrefl [b]

[a] Univ. Grenoble Alpes, CEA, Liten, DTNM, Grenoble 38000, France
[b] Department for Integrated Sensor Systems, University for Continuing Education Krems, Viktor Kaplan Straße 2E, 2700 Wiener Neustadt, Austria
[c] Univ. Grenoble Alpes, CNRS, Institut Neel, Grenoble 38000, France

ARTICLE INFO

Keywords:
Permanent magnets
1–12 compounds
Microstructure
Micromagnetics

ABSTRACT

$Nd(Fe,Mo)_{12}$ compounds have been considered as promising candidates for next generation permanent magnet materials, thanks to their excellent intrinsic hard magnetic properties, comparable to those of the well-known NdFeB magnets, allowing a minimum usage of rare earth elements (RE). However, achieving high coercivity in an anisotropic microstructure has proven to be a significant challenge, which hinders their practical applications. In this work we present microstructural studies of the strip-cast $Nd(Fe,Mo)_{12}$-based alloy. Detailed microstructural characterization using high resolution transmission electron microscopy (TEM) reveals submicron sized 1–12 magnetic grains, indicating that the addition of Cu leads to grain boundaries segregated into RE and Cu. Micromagnetic simulations based on the observed microstructure emphasize the role of grain boundaries and of crystalline defects on the development of coercivity. This work provides evidence about relevant aspects of the microstructure of these compounds that is correlated to the coercivity development.

1. Introduction

The intensive use of rare earth elements (RE) is required in a vast spectrum of emerging key technologies like wind turbines or electric transportation, among others. As such, we experience a big pressure on the market of these critical elements that will only quickly increase in the upcoming years. This will affect the production of RE-based high performance permanent magnets, whose demand will rapidly grow within the next decade, in order to comply with the transport electrification and the wind energy deployment [1]. Thus, the replacement of Nd-Fe-B magnets by rare earth free [2], rare earth lean [3] or reducing the use of critical-rare-earth compounds [4] has become a matter of premier interest. Significant research activity has been devoted over the last decade to find alternative materials with similar, or even better, magnetic properties compared to the reference NdFeB magnets. The development of RE-free or RE-lean permanent magnets would be a great step-forward in terms of cost reduction and supply reliability [5].

Intermetallic $RE\text{-}Fe_{12}$ compounds, with tetragonal $ThMn_{12}$-type crystal structure, are known from more than 30 years [3] and are considered as the most promising candidates for the substitution of the NdFeB permanent magnets, thanks to their relatively high Curie temperature (T_C), saturation magnetization (M_s) and magnetocrystalline anisotropy (MAE) [3]. The tetragonal $ThMn_{12}$–type structure of the 1–12 compounds without stabilizing elements was obtained only in thin-films with thicknesses up to 360 nm [6,7], whilst in its bulk form they can only be stabilized thanks to a partial substitution of Fe by other metallic elements, such as Ti, V, Cr, Mo, among others.

Different compositions of the $REFe_{12-x}M_x$ system have been studied, regarding different RE elements and the nonmagnetic stabilizing element (M) [8–19]. Most studies have focused on the $Sm(Fe,M)_{12}$ based compounds over the last decade, as it presents high uniaxial anisotropy at room temperature. A rather exhaustive investigation aiming to the development of the extrinsic magnetic properties of Sm-based 1–12 compounds (namely coercivity and remanence), resulted in significant progress in coercivity increase [11,12,20]. Nevertheless, the remanent magnetization remains low, if compared to NdFeB magnets. In addition, Sm-based 1–12 compounds have the advantage of holding high uniaxial anisotropy at room temperature, without the need for structural modifications through the insertion of light atoms. The investigation of the Nd-based 1–12 compounds as permanent magnets is of great interest, Nd

* Corresponding author.
E-mail address: sorana.luca@cea.fr (S. Luca).

https://doi.org/10.1016/j.jallcom.2024.178039
Received 14 October 2024; Received in revised form 27 November 2024; Accepted 9 December 2024
Available online 10 December 2024

being more abundant in the Earth's crust compared to Sm. However, $NdFe_{12-x}M_x$ exhibits a weak uniaxial anisotropy at room temperature, dominated by the iron sub lattice [21], making it necessary to incorporate interstitial modifications by insertion of light elements, like H, B, C or N. As a consequence, not only the magnetocrystalline anisotropy is enhanced, but also the remanent magnetization and Curie temperature [22].

$Nd(Fe,Mo)_{12}$ is stable in a wide temperature range (from 600 to 1100 °C) [23], [24], and can be fabricated by different techniques like book mold, melt spinning or strip casting. Among the interstitial modified $Nd(Fe,M)_{12}$ alloys, nitrided $Nd(Fe,Mo)_{12}$-based compound have been considered as a promising material for permanent magnet applications, with a Curie temperature $T_C \sim 320°C$, high saturation magnetization M_s (up to 1 T) and large magnetocrystalline anisotropy H_a (up to 11 T) [10]. Despite these quite interesting intrinsic magnetic properties, coercivity is still low for permanent magnet applications [16, 25]. Understanding the formation of the 1-12 structure and the existence of competing phases, as well as of the nitrogenation process, is essential to obtain a high purity precursor, which is a prerequisite to increase the intrinsic magnetic properties. In addition to this, the relationship between microstructure and the extrinsic magnetic properties of the material is an important factor for the development of the performance of the final permanent magnet.

The coercivity mechanism in the 1–12 compounds is of nucleation-type [19,26] similar to the benchmark NdFeB magnets. It is generally influenced by the grain size and the magnetic decoupling of the grains thanks to a non-magnetic grain boundary phase. For instance, in $Sm(Fe,M)_{12}$ magnets, it was demonstrated that the optimization of the grain boundary phase contributes to the enhancement of coercivity [11,12]. In the case of Nd-based nitrides the influence of grain boundary phases has not yet been greatly investigated, mainly due to the fact that the incorporation of nitrogen dramatically reduces the decomposition temperature of the nitrided alloy, which is of 657°C for $Nd(Fe,Mo)_{12}N_x$ [27]. The typical coercive field ($\mu_0 H_c$) of $NdFe_{10.5}Mo_{1.5}N_x$ powders obtained from strip-cast alloys, is around 0.5 T [25], still far below the feasible limits considering the Brown paradox ($\sim$ 30 % of H_a).

Though, maximum performances, i.e. maximum coercivity values, are expected for dense materials, which cannot be produced by traditional sintering methods of nitrided Nd-based compounds. In addition, the lack of suitable grain boundary phases, capable of magnetically decoupling adjacent 1–12 grains, also contributes to the low coercivity values registered up to now. In addition, the presence of macroscopic and microscopic defects can also hinder the development of the coercivity. Thus, investigating the influence of grain boundary phases in Nd-based 1-12 alloys (and their nitrides) together with crystalline defects, offers the opportunity to identify an appropriate microstructure to enhance $\mu_0 Hc$ above the values reported so far.

In the present work, we investigate the particular microstructure of the $Nd(Fe,Mo)_{12}$-based strip cast alloys. We chose a composition in the stability range of the 1–12 phase at temperatures between 600 and 1100°C, with the addition of Cu and an excess of Nd to allow the formation of a grain boundary phase insulating adjacent 1–12 grains. To understand the relationship between the microstructure and the magnetic properties, different length-scale analysis were conducted. The observed magnetic properties are compared to those obtained by micromagnetic simulations. The latter were performed based on our microstructural observations, for a more realistic modelling.

2. Experimental procedure

Alloys with nominal compositions $(Nd_{0.75},Pr_{0.25})_{1.25}Fe_{10.5}Mo_{1.5}Cu_{0.1}$ (hereafter referred as Cu-rich $Nd(Fe,Mo)_{12}$) were prepared by strip-casting (SC) technique, with wheel speed of 1.43 m/s under a controlled atmosphere of 300 mbar of Ar. As-cast alloy flakes, having a mean thickness of 287 ± 61 μm, were ball milled to coarse powder for X-ray diffraction (XRD). XRD patterns were acquired at room temperature in a Bruker D8 Advance, with Cu $K\alpha_1$ radiation, at 2θ angles between 20 and 90°, with a step of 0.005° and counting time of 3 s/step.

Thermomagnetic measurements were carried out on a homemade magnetic torque balance on non-oriented powders, sealed in a quartz tube under inert gaz. Magnetization response as a function of the temperature was measured upon heating from 30 to 850 °C.

Isothermal magnetization measurements were performed on magnetically aligned nitrogenated jet mill powders, embedded in epoxy resin and encapsulated in a Teflon mold, submitted to a magnetic field of 7 T for 12 h, during the solidification of the resin.

Nitrogenation experiments were conducted on fine monodisperse jet milled powders (with a mean grain size D50 = 7.8 μm), at temperatures between 300 and 500°C, under 100 kPa of nitrogen gas, using a Sievert-type volumetric apparatus from HERA.

Microstructure observation was firstly performed by scanning electron microscopy (FEG-SEM, Zeiss Merlin) on resin-embedded flakes with a polished surface to 0.04 μm colloidal silica. Submicron scale observations were performed by transmission electron microscopy (TEM), using Bright Field (BF) and High Angle Annular Dark Field (HAADF) detectors. Scanning transmission electron microscopy (STEM) investigations and high resolution TEM (HRTEM) observations were conducted with a Thermo-Fisher Osiris Tecnai instrument, equipped with an X-FEG source and operating at 200 kV. Energy dispersive X-ray spectroscopy (EDX) was employed in STEM mode thanks to the Super-X EDX system. EDX hyper-maps were acquired with Esprit 1.9 software (Bruker). Crystal orientation was investigated thanks to the Automated Crystallographic Orientation Mapping (ACOM) [28]). The software Astar™ from Nanomegas was used to index the diffraction patterns and to determine the orientation of the different phases. Diffraction patterns were acquired without precession with a beam size of about 2 nm and 28 nm pixel. TEM sample was lifted out by focused ion beam (Zeiss CB-550) and placed on a Mo grid.

Micromagnetic simulations were conducted to compute the demagnetization curve of granular microstructures. The magnetic states along the demagnetization curve are obtained by consecutive energy minimization steps [29], starting from a positive external field in the range of the anisotropy field of the given phase, in steps of –2 mT. The magnetic material and an airbox surrounding the magnet were discretized with tetrahedral finite elements. The resulting algebraic minimization problem was solved with a preconditioned conjugate gradient solver [30]. The airbox serves as a simple but effective method to treat the open-boundary problem [31], when algebraic multigrid solvers are used on graphical processors [32].

We created three variations of the granular structure of the magnet, two with 20 grains and one with 60 grains within a 700x700x700 nm^3 cube. The extensions of the model were chosen close to the limits of the available hardware for these computations. We used the software Neper with the grain-growth morphology option to define the shape of the grains. This option allows for a wider grain size distribution and higher grain sphericities compared to Voronoi tessellations [33,34]. The average grain size was around 258 nm (min. 120 nm, max. 400 nm) for the models with 20 grains and around 179 nm (min. 69 nm, max. 326 nm) for the model with 60 grains. Grain boundaries, defects and twin planes were drawn with the software package Salome [35] and then meshed within the SMESH module of Salome using MeshGems [36]. The mesh size was chosen in the range of the Bloch parameter of the hard magnetic main phase $\delta_0 = \sqrt{A/K_u} = 2.7$ nm, which resulted in finite element meshes with approximately 15 million to 16 million nodes or 90 million to 100 million tetrahedrons. A is the exchange constant and K_u the uniaxial anisotropy constant of the main phase. The thickness of the grain boundary was 7 nm which adds up to a volume share in the range of 4 % for the 20 grains model rising to 7 % for the model with 60 grains.

The uniaxial anisotropy constant K_u and saturation magnetization M_s of the main phase $Nd(Fe,Mo)_{12}N$ were derived from the experimental

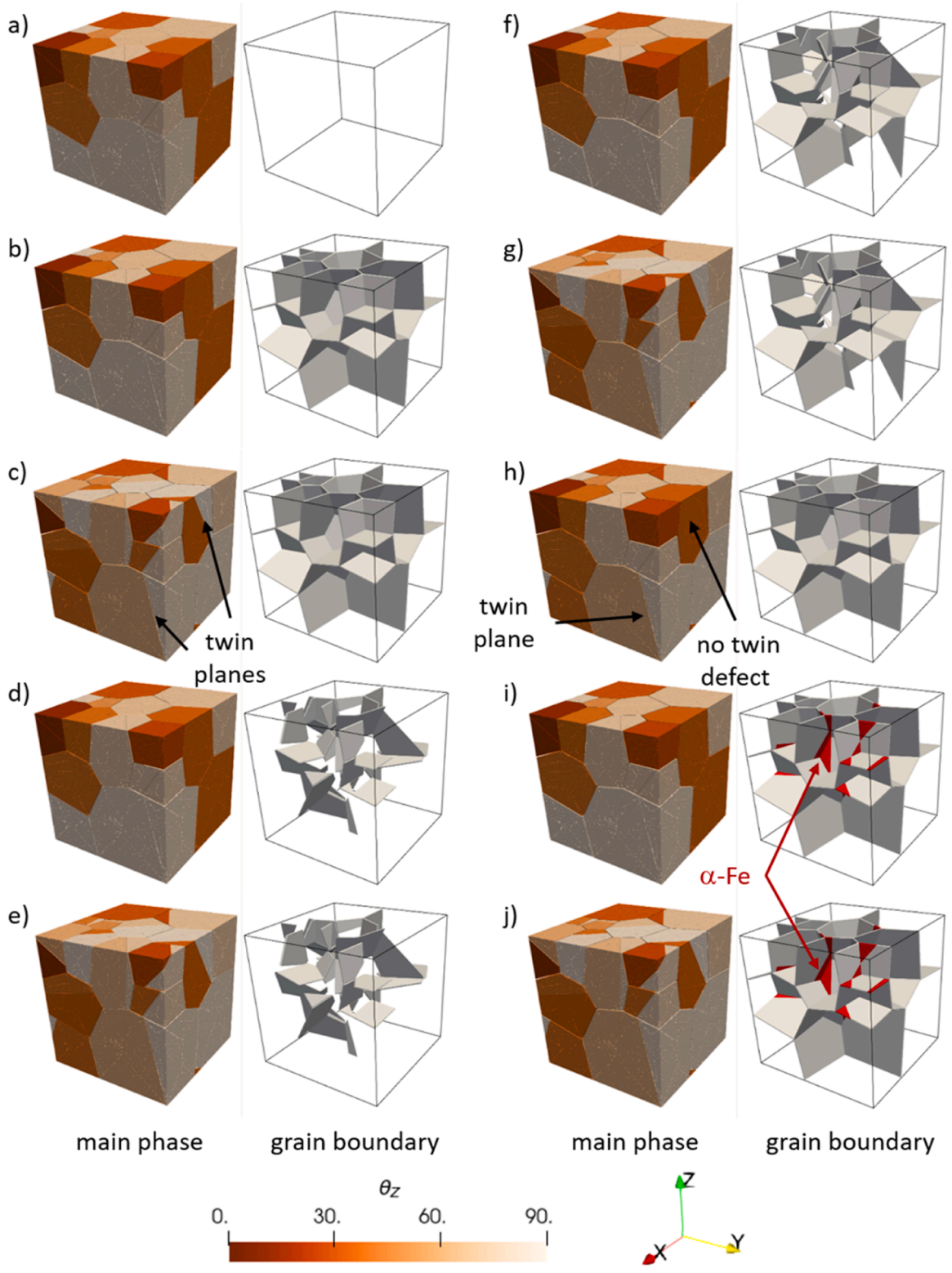

Fig. 1. The images show the 10 scenarios a) to j) for one of the model geometries with 20 grains. The images in the second and fourth column show the 7 nm thick nonmagnetic grain boundary in grey. The grain boundary images and comparing simulation scenarios differing only in the presence of twinning defects, e.g. compare b) to c), may help to identify grain shapes and twinnig planes. Twinning planes are visible due to the color change within a grain, which denotes a change of the easy axis orientation within a grain. The color scale for the images in the first and third columns shows the misalignment of the easy axes with respect to the z-axis in degrees.

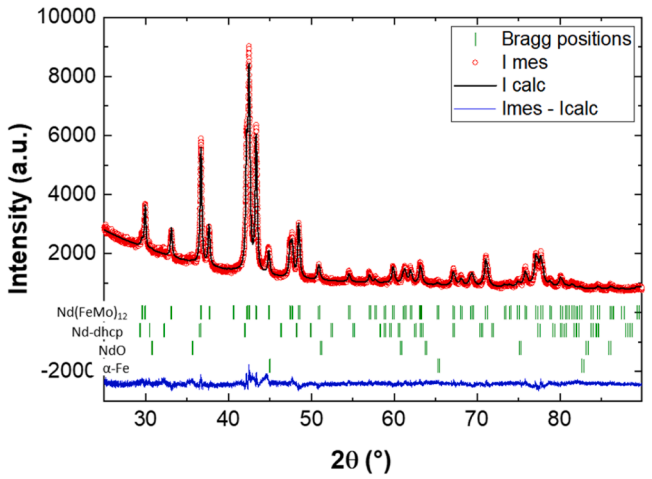

Fig. 2. XRD pattern and Rietveld refinement of Cu-rich $Nd(FeMo)_{12}$ powder. Bragg positions of the identified phases, from top to bottom, are tetragonal Nd $(FeMo)_{12}$ (> 99 %) with cell parameters a = 0.8598 nm and c = 0.4798 nm, and less than 1 % of dhcp-Nd with cell parameters a = 0.3665 nm and c = 1.1796 nm, cubic NdO with cell paramets a = 0.5065 nm and α-Fe.

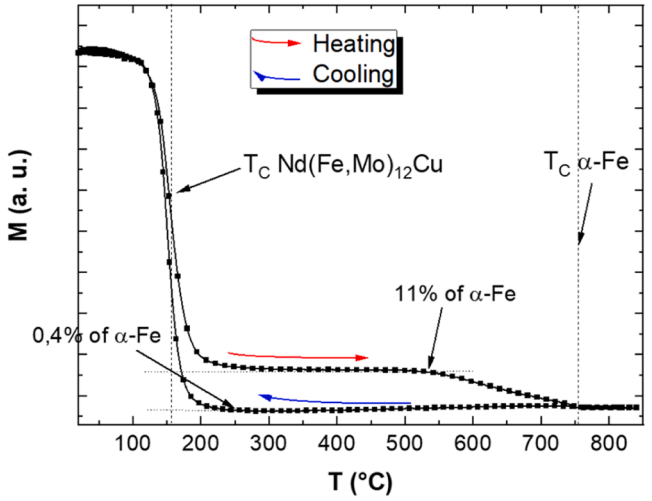

Fig. 3. Thermomagnetic measurements of jet milled powders of as-cast Cu-rich $Nd(Fe,Mo)_{12}$. The magnetizations is given in arbitrary units.

results. K_u was calculated from the anisotropy field. $K_u = 4.38$ MJ/m^3 and $\mu_0 M_s = 1$ T. The exchange constant $A = 32$ pJ/m was taken from literature [10]. The intrinsic properties of α-Fe were set to $K_u = 0$, $\mu_0 M_s = 2.15$ T and $A = 21$ pJ/m. For nonmagnetic phases those three constants were set to zero.

We defined ten simulation scenarios, created three variants of the granular model geometries and applied the external field in three different directions, which gave a total of 90 simulations. Nine demagnetization curves per scenario were summarized in one averaged curve. The 30 simulations per geometry all used the same finite element mesh. The simulation scenarios were realized by changing the intrinsic properties of geometric features identified by tagged elements of the mesh. We kept the changes minimal to be able to compare the different scenarios.

The tessellation for 20 grains was used twice to create two granular models with the same grain shapes but different random orientations of the twin planes. The tessellation for 60 grains was used only once. The orientation of the twin planes defined the orientation of the easy axes. An isotropic distribution for the orientations of the easy axes was targeted. The angle between the easy axes of two variants of a grain with twin defect was given by 122° to match the experimentally measured twin angle of 58° (180°-122°). Each grain was split by a randomly oriented twin plane into two halves. For the random orientation of the twin planes we used sphere-point-picking [37]. To give the basic distribution

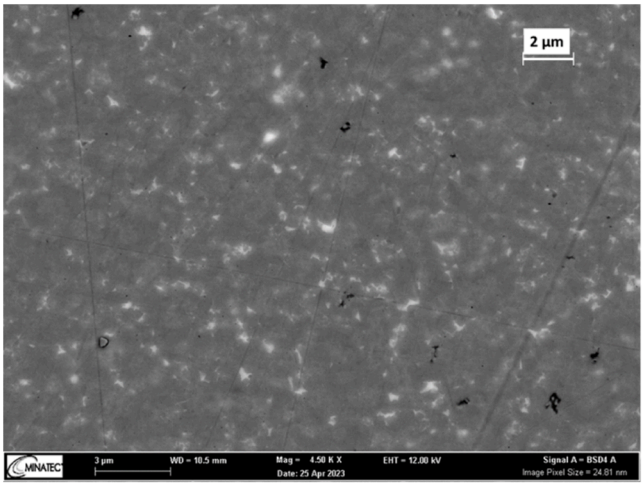

Fig. 5. SEM-BSE image of the Cu-rich $Nd(Fe,Mo)_{12}$ flakes - polished section.

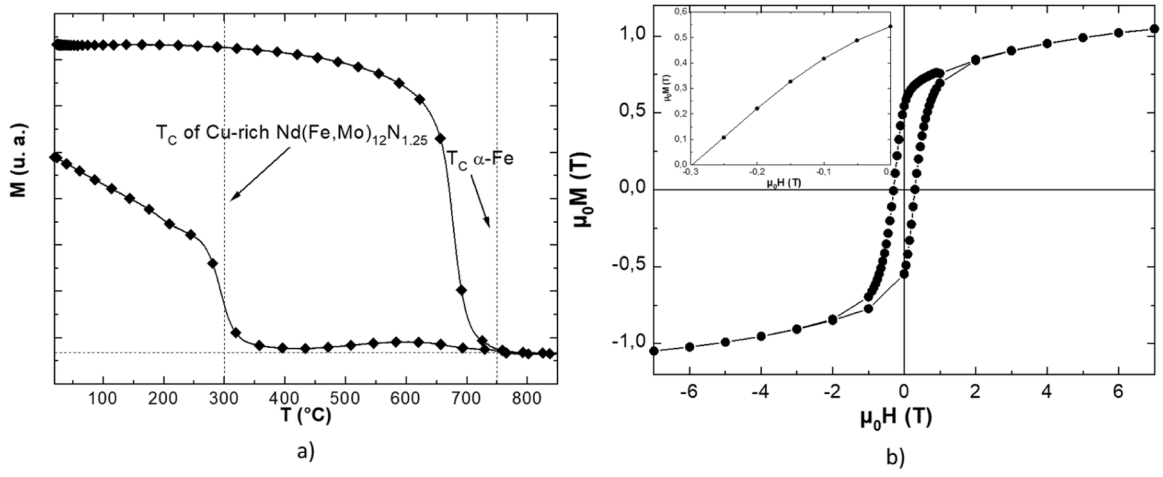

Fig. 4. a) Thermomagnetic measurements of jet milled Cu-rich $Nd(FeMo)_{12}N_{1.245}$ powders, nitrided at 350°C under 100 kPa of nitrogen gas. b) Room temperature M (H) curve of jet milled Cu-rich $Nd(FeMo)_{12}N_{1.245}$ aligned powders.

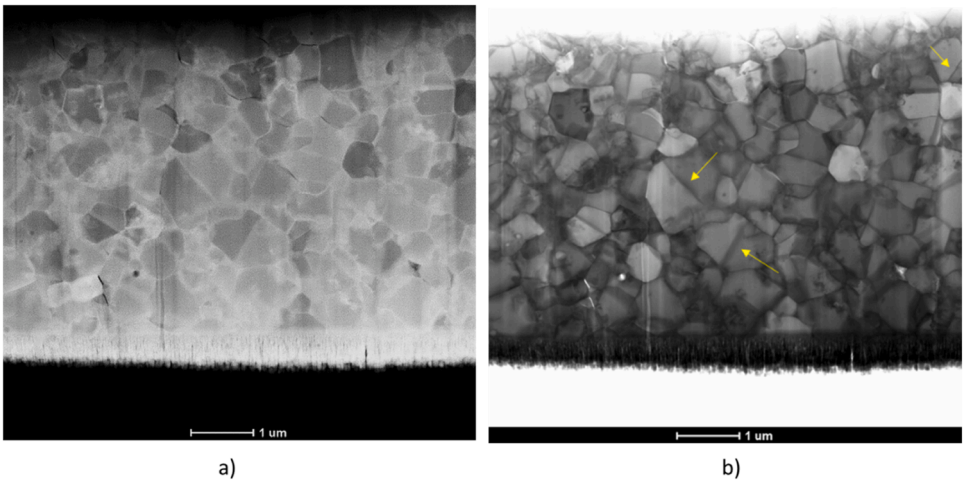

Fig. 6. a) HAADF-STEM and b) BF-STEM images of the Cu-rich $Nd(Fe,Mo)_{12}$ flakes.

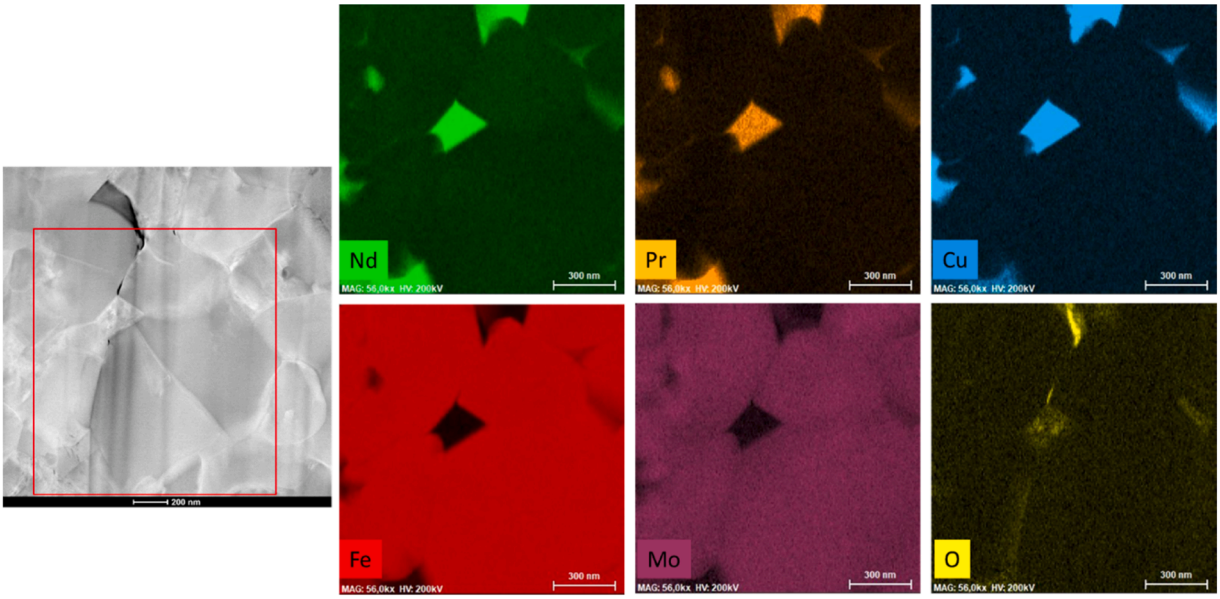

Fig. 7. Nd, Pr, Fe, Mo, O and Cu EDX maps of Cu-rich $Nd(Fe,Mo)_{12}$ flakes.

of the easy axes, the two easy axis vectors per grain were then rotated + /- 61° out-of-plane to get an angle of 122° between the easy axes of the two variants of a grain with twin defect. For scenarios with grains without twin defects one of the two easy axes of the variants defined the easy axis for that grain.

Due to the small number of grains and hence poor statistics to model an isotropic magnet, we applied the external field along the x, y and z directions, respectively, to increase the number of simulations. By comparing the remanence magnetization of those simulations to the expected value of 0.5 M_s we checked if the setup of the simulations was suitable. The external field was decreased from the positive anisotropy field $\mu_0 H_a = 11$ T in −2 mT steps. Nine computed demagnetization curves per simulation scenario (3 different geometries, times 3 different external field orientations) were summarized into one averaged curve.

The ten simulations scenarios were defined with the following properties, mainly different in the nature of the grain boundary phase and the presence of twin defects (see Fig. 1). Most of the scenarios except for a) and h) come in pairs to identify the effects of twin defects. The range in the volume shares and number of affected grains is a consequence of the three model geometries.

a)Exchange-coupled grains.

b)Grains separated by a 7 nm thick nonmagnetic grain boundary.

c)Same as b) but grains with twinning defects.

d)Grains partially separated by a 7 nm thick nonmagnetic grain boundary. Only 30 % to 37 % of the grain boundary volume defined in b) is nonmagnetic.

e)Same as d) but grains with twinning defects.

f)Grains partially separated by a 7 nm thick nonmagnetic grain boundary. 63 % to 70 % of the grain boundary volume defined in b) is nonmagnetic.

g)Same as f) but including grains with twinning defects.

h)Mix of b) and c). Only grains larger than the average grain size of the model show twinning defects. In total, 6 out of 20 or 18 out of 60 grains are with twinning defects.

i)Same as b) but parts of the nonmagnetic grain boundary were replaced by α-Fe. α-Fe properties were assigned to 5 % to 7 % of the volume of the grain boundary in b) which corresponds to about 0.2 % to 0.5 % of the total volume of the model.

j)Same as i) but including grains with twinning defects.

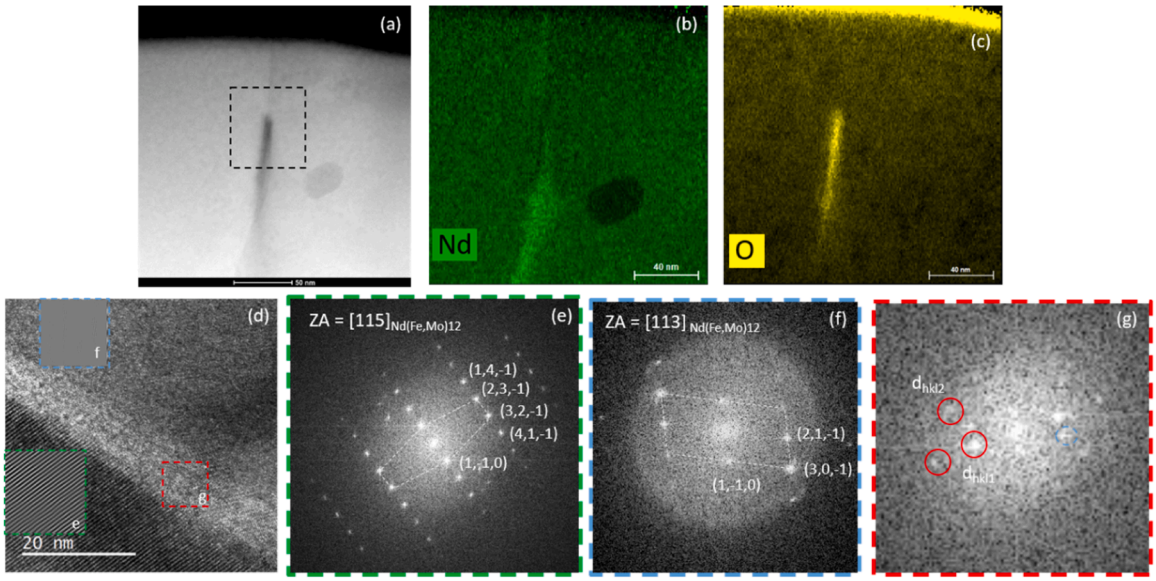

Fig. 8. Analysis of a grain boundary phase. (a) HAADF STEM images on the Cu-rich Nd(Fe,Mo)$_{12}$ flakes.(b) and (c) Nd and O EDX maps. (d) HRTEM image of the same grain boundary. (e) Frourier Transform of the grain designated by a green square and oriented along [115] zone axis. (f) Frourier Transform of the grain designated by a blue square and oriented along [113] zone axis. (g) Frourier Transform of the phase at grain boundary.

3. Results and discussions

3.1. Structural analysis, intrinsic and extrinsic magnetic properties

Fig. 2 presents the graphical result of a Rietveld refinement of XRD pattern of the Cu-rich Nd(Fe,Mo)$_{12}$ powders. Three different phases were identified: 99 % of $NdFe_{10.5}Mo_{1.5}$, less than 1 % of cubic NdO_x (space group Fm-3m) and metallic *dhcp* Nd (space group P 63/mmc). α-Fe was added to the Rietveld refinement in Fig. 2, however it was not detected, mainly due to superposition of its Bragg reflections to those of 1–12 phase, and to the tiny size of α-Fe crystallites (dendritic structure), contributing with very low intensity broad-peaks to the total diffraction pattern.

Magnetic measurements of non-nitrogenated powders (not shown here) reveal, as expected, low anisotropy field, $\mu_0 H_a = 2$ T (estimated from crossing point of M(H) curves measured parallel and perpendicular to the easy magnetization axis) and hence very low coercivity. The measured saturation magnetization is $\mu_0 M_s = 1$ T, consistent with previously reported values [10]. Thermomagnetic measurements on coarse powders exhibit one magnetic transitions at 155°C, corresponding to the 1–12 phase and a second one, only visible on heating, ranging from 550°C to around 770°C, corresponding to α-Fe (see Fig. 3). An amount of 11 wt% of α-Fe is estimated by comparison with the measurement of a piece of pure iron. Even though this phase is not detected with the XRD measurements, its presence is clearly evidenced with these measurements and was already identified in similar 1–12 compounds [38], and can be under the form of very small size crystallites and/or a poorly crystalized phase. The magnetic transition corresponding to the Curie temperature of α-Fe almost disappears upon cooling to room temperature, indicating that a recombination of α-Fe and free Nd take place between 550°C and 800°C. The estimated remaining amount of α-Fe is 0.4 wt%.

Following this result, as cast flakes were annealed at 850°C during 10 minutes and then jet milled to monodisperse powders of 7.8 μm mean grain size, prior to nitrogenation at 350°C and 100 kPa of N_2 gas, up to nitrogen uptake of 1.245 N atoms. Here we consider a nitrogen content of 1 corresponding to 1 N atom/unit formula of 1–12 phase, in the hypothetical case where the intergranular RE-rich phase does not absorb any nitrogen. The thermomagnetic measurements of jet milled nitrogenated powders show a single magnetic transition near 300°C on heating, corresponding to the Curie temperature of the nitrogenated 1–12 phase (Fig. 4a), confirming a complete nitrogenation of the 1–12 phase. The magnetization curve shows a slight increase at around 600°C, indicating the decomposition of the nitrogenated powders with the subsequent formation of a soft ferromagnetic phase, certainly the α-(Fe-Mo) solid solution. This is corroborated by the fact that, upon cooling down to room temperature, only one magnetic transition is observed at nearly 700°C, meaning a complete decomposition of the 1–12 nitride. This was already reported in jet mill Nd(Fe,Mo)$_{12}$ nitrogenated powder [38].

Despite a large anisotropy field of $\mu_0 H_a \sim 11$ T of the nitrogenated powders (estimated from crossing point of M(H) curves measured parallel and perpendicular to the easy magnetization axis), coercivity values remains rather low (< 0.3 T) for permanent magnet applications (see insert of Fig. 4b).

In sum, fully nitrogenation of the 1–12 structure allows to greatly enhance both Curie temperature, from 155°C to 300°C and the anisotropy field from 2 T to 11 T. It also leads to the enhancement of the saturation magnetization from 1 T to 1.1 T, ascribed to the modification of the 3*d* band electronic structure of Fe [39].

3.2. Microstructural analysis

The microstructures of the alloys have been firstly observed by SEM. Collected backscattered electrons are sensitive to atomic number, giving rise to chemical contrast to the images. The observed dark-grey phases (with grain size < 1 μm) may correspond to the 1–12 phase and light-gray ones to Nd-rich phases (metallic Nd and Nd-oxide) (Fig. 5). With the contrast achievable with the SEM, it can be noticed that the Nd-rich phase is not uniform within the flake, but rather concentrated in pockets. The desired grain boundary phase completely surrounding 1–12 grains is not detectable at this scale of analysis, either because of its small thickness or because of its non-uniform repartition around the grains. Black spots on the image represents closed porosity on the flakes.

To further characterize the microstructural features of the flakes and especially the distribution and composition of the intergranular phase, STEM-EDS have been employed. The observation of TEM sample in HAADF and STEM-BF mode (Fig. 6) reveals a microstructure constituted of fine grains, between 50 and 1000 nm. The presence of structural defects inside the grains are pointed out by arrows in Fig. 6b.

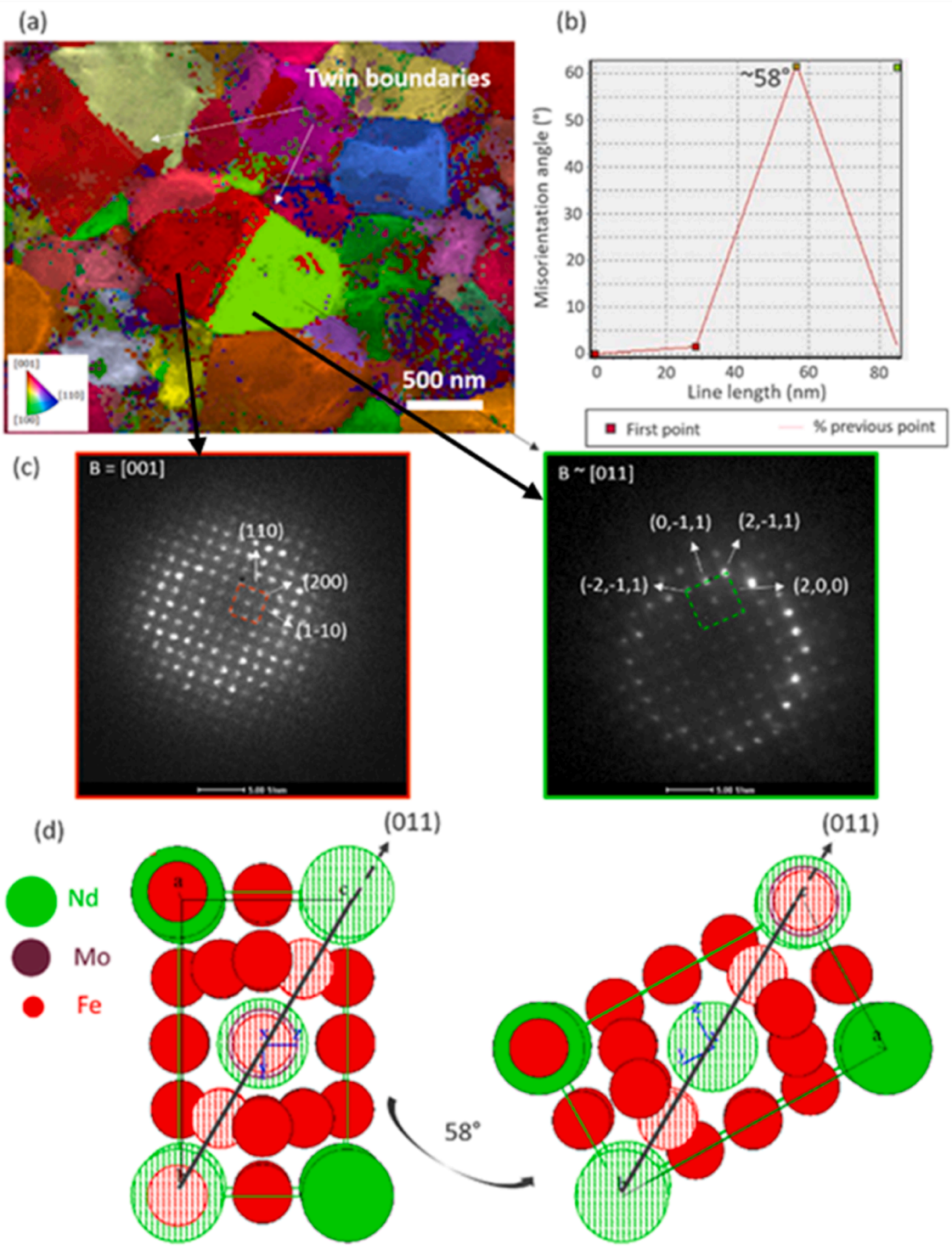

Fig. 9. (a) Inverse Pole Figure, IPF-z (beam direction normal to the sample surface), showing the presence of twinned grains in $Nd(Fe,Mo)_{12}$ phase with the tetragonal ThMn12 - type crystal structure. (b) Misorientation angle profile across a twin boundary. (c) Diffraction patterns on either side of the twin boundary pointed out by black arrows and (d) the corresponding schematic representations of the crystal lattices.

EDX Nd, Fe, Mo and Cu elemental maps of Cu-rich $Nd(Fe,Mo)_{12}$ grains, triple grain junctions and non-uniform grain boundaries are shown in Fig. 7. It confirms that Cu is not present in the $Nd(Fe,Mo)_{12}$ main phase, only in the grain boundary phase or the triple junctions, together with the excess of RE. On the other hand, Fe and Mo locate preferentially into the 1–12 grains. The exact composition of the grain boundary phase was not determined in this study, however relatively low Fe contents in the grain boundary have already been reported in Nd $(Fe,Mo)_{12}$ melt spun ribbons [40], suggesting a paramagnetic feature of the grain boundary phase. Some of the thin grain boundary phases are Nd/Pr and Cu segregated however not all the grain boundaries present RE or RE-Cu enrichment. It is thus evidenced that magnetic 1–12 grains may be magnetically coupled, which in principle hinders the development of coercivity.

In Fig. 8a, b and c are shown HAADF-STEM images, associated with Nd and O EDX maps of a grain boundary which contains a Nd oxide. The

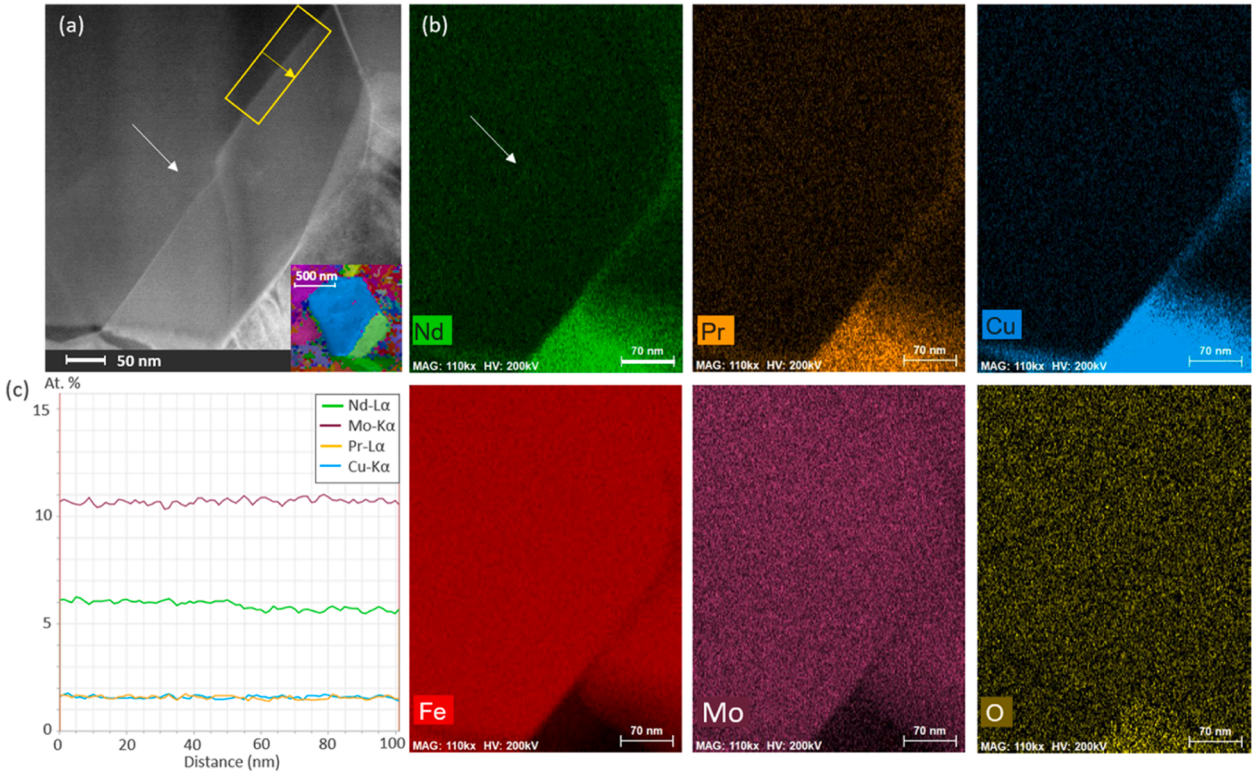

Fig. 10. Chemical analysis of a twinned 1–12 grain. (a) HAADF-STEM image with its corresponding IPF-z map. (b) Nd, Pr, Cu, Fe, Mo and O EDX element maps. (c) chemical profile across the twin boundary as pointed out in the yellow rectangle in (a) (mean amount of Fe is 75 at%).

Fourier Transform patterns of this same region are presented in Fig. 8.d, e, f and g. Both grains on either side of the grain boundary were indexed according to the tetragonal $ThMn_{12}$–type structure (space group I4/mm) with lattice parameters $a = 0.85917$ *nm* and $c = 0.47954$ *nm*, consistent with the values obtained from XRD analysis $a = 0.85982$ *nm* and $c = 0.47985$ *nm*. The Fourier Transform pattern of the grain boundary at point g revealed two planes with $d_{hkl1} = 0.319$ nm and $d_{hkl2} = 0.198$ nm and 36° between them. They can be indexed as (-1 1 1) and (-2 2 0) planes of the NdO_2 phase, which displays a face centered cubic structure with lattice parameters $a = 0.554$ *nm*, also comparable to XRD values ($a = 0.5065$ *nm*). This phase, paramagnetic at room temperature, is not harmful for the development of the coercivity. Small amount of it has proven to be even beneficial for coercivity and corrosion resistance improvement in NdFeB permanent magnets [41].

Fig. 9 shows an inverse pole figure (IPF) map evidencing grains with different crystal orientations. The IPF was indexed, thanks to ACOM-TEM, as $Nd(Fe,Mo)_{12}$ phase with a tetragonal $ThMn_{12}$ - type crystal structure. Misorientation indicating twin-like crystal defects are observed in some grains, pointed by arrows in Fig. 9a, also pointed out in Fig. 6b. These defects are observed in grains of different size order, starting from a few hundreds of nm up to micrometer size. The IPF along z axis (parallel to the electron beam) and the misorientation angle profile across the twin boundary show a misorientation angle of approximately 58° on either side of the twin boundary plane, corresponding to {011}-type plane. This value is consistent with previous reports showing the presence of twins in 1–12 intermetallics [42,43].

To highlight any element segregation at the twin boundary, fine EDX-TEM profiles have been performed across the twin boundaries of different grains. For that, the TEM specimen was oriented to observe the {011} twin plane quasi parallel to the electron beam in order to maximize the chance to detect a potential segregation at the twin boundary. As an example, in Fig. 10 we show the 2D compositional map of Nd, Pr, Cu, Fe, Mo and O of one twined grain (surface analyzed = 250 ×400 nm) with its corresponding HAADF-STEM image.

With the resolution of the analysis performed (beam size of about 1 nm and pixel size of 5 nm), no evidence of element segregation on the twin boundary was detected, contrary to what has already been observed by Atom Probe Analysis in other 1–12 systems [42,43]. We have analyzed several twined grains (not shown here) however no evidence of element segregation has been detected at the twin boundaries in any of them.

3.3. Micromagnetic simulations

In our simulations the sample size is much smaller than in experiment, causing an underestimation of the effects of demagnetizing fields. In fact, simulations with different micromagnetic models show that the coercive field decreases with increasing sample size [44]. Therefore, it is expected that critical fields obtained from simulations to be higher than values obtained from the actual experiment.

As a reminder, we defined ten simulation scenarios, created three granular model geometries and applied the external field in three different directions, which gave a total of 90 simulations. Nine demagnetization curves per scenario were summarized into one averaged curve labelled a) to j).

Fig. 11i shows the demagnetization curves for the scenarios without any twinning defects. The curves show the typical behavior of isotropic magnets with remanent magnetization M_r close to 0.5 M_s. Reversible rotation of the magnetization occurs in a wide range of the applied external field. It can be noticed that an external field equal to the anisotropy field (11 T) is not enough to saturate the magnet but resulted in a magnetization of 0.92 M_s which is close to the value computed by Stoner and Wohlfarth for randomly oriented non-interacting particles [45].

The critical field at which irreversible switching starts changes with defects and the nature of the grain boundary phases. In [46] the coercive field was defined as the field of maximum susceptibility in the demagnetization curve. We define the switching field H_{sw} as the value of the

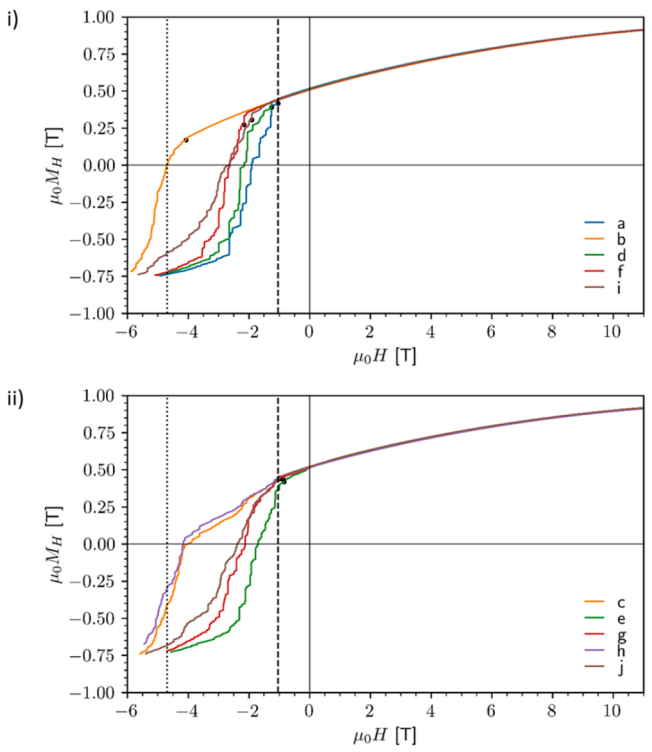

Fig. 11. Averaged demagnetization curves for i) scenarios with grains without twin defect and ii) scenarios with grains with twin defect. Curves with the same color compare scenarios with the same grain boundary configuration and differences thus show the impact of twinning defects. The black round markers denote the switching fields H_{sw} as defined above. The dashed and dotted vertical lines in both figures denote the switching field of scenario a) and the coercive field of scenario b), respectively, to ease comparison of the results.

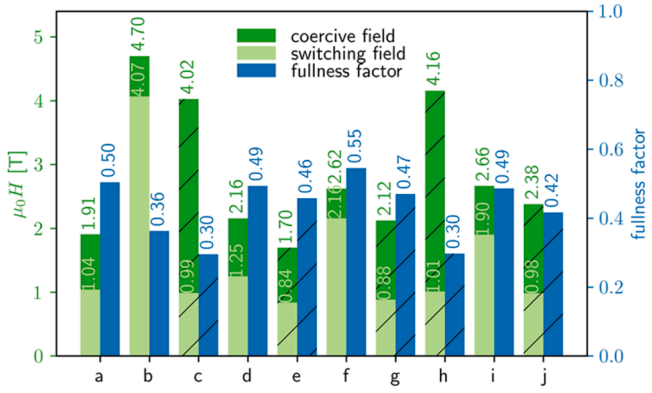

Fig. 12. Comparison of absolute values of switching field and coercive field (green) and fullness factor (blue) for all scenarios. Hatched bars mark scenarios with grains presenting twin defects.

external field where the difference quotient $dM_H/dH > 4$ for the first time along the averaged demagnetization curves. M_H is the magnetization parallel to the applied external field H. This switching field represents the first irreversible switching of the magnetization of grains or parts of grains. The threshold value 4 was chosen to ignore outliers in any out of nine simulations forming an averaged demagnetization curve. H_{sw} is shown in Fig. 11 as black markers. We define the coercive field H_c as the value of the external field where $M_H \leq 0$.

The best switching field is found for scenario b), where all grains are exchange decoupled by a non-magnetic grain boundary phase. For this "best-case" microstructure within the defined scenarios of these micromagnetic simulations the switching field is $\mu_0 H_{sw} = 4.07$ T, which is 37 % of the anisotropy field ($\mu_0 H_a = 11$ T). The coercive field is $\mu_0 H_c = 4.7$ T, which is 42.7 % of the anisotropy field. Demagnetizing fields and magnetostatic interactions reduce the coercive field compared to the 48 % of H_a obtained from the Stoner-Wohlfarth model for non-interacting isotropic particles [45]. Exchange coupling between grains (scenario a) reduces the switching field by $\Delta\mu_0 H_{sw} = 3.03$ T. This effect is caused by a partial domain wall formed at the grain boundary that acts as a defect easing the nucleation of a reversed domain [47]. The switching field for scenario a) is $\mu_0 H_{sw} = 1.04$ T, which represents 9.5 % of the anisotropy field and the coercive field is $\mu_0 H_c = 1.91$ T, which represents 17.4 % of the anisotropy field. Scenario a) defines the "worst-case" in terms of H_{sw} and H_c within this set of simulations shown in Fig. 11i. In scenarios d), f), and i) the grains are only partially exchange-decoupled by a non-magnetic grain boundary. The switching fields improve by 20 % to 108 % compared to scenario a) and the coercive fields improve by 13 % to 39 % compared to scenario a). In scenario i), 5 % to 7 % of the non-magnetic grain boundary volume (0.2 % to 0.5 % of the total volume) was replaced with α-Fe, randomly distributed within the grain boundary phase (see Fig. 1i). Despite the small volume fraction of the soft magnetic phase this scenario conducts to a reduction of the switching field of about 50 % compared to scenario b). It can be attributed to exchange coupling of the grains through α-Fe that conducts to switching field reduction owing to the presence of soft magnetic phase. The thickness of the soft magnetic phase is only 7 nm (same as grain boundary thickness) but it exceeds the critical dimension of soft phases as calculated by Kneller and Hawig [48].

Figure 11ii shows the demagnetization curves for the scenarios with twin defects. In a previous study, micromagnetic simulations were presented showing that the switching field of an isolated $SmFe_{11}Ti$ grain with twin defect (similar twinning angle) was less than 0.4 H_a considering various alignments with respect to the external field [42]. In [49], studying twin defects in MnAl-C, the switching field with respect to the orientation of the external field was plotted on the surface of a unit sphere. For an isolated spherical grain with twin defect (true coherent twin) the switching fields were below 0.5 H_a for most external field orientations. In this work we investigate the impact of the presence of multiple twined grains in isotropic magnets. We observe that the first nonreversible switching event in any of the twinned-grains scenarios happens earlier or at similar external fields than for the "worst-case" scenario a) regardless of all the effort that is put into creating a nonmagnetic grain boundary. This is visible in Figure 11ii as all black round markers denoting the switching fields appear right of the dashed vertical line marking the switching field of scenario a). If all grains are exchange-decoupled by a nonmagnetic grain boundary (scenarios c) and h)) magnetization reversal starts at twin boundaries. This nucleation effect is similar to misoriented exchanged coupled grains, in which partial domain walls form at the interfaces. Introducing a non-magnetic grain boundary, that hinders the propagation of reversed domains, improves coercivity. While it also improves the switching field for scenarios without twin defect, in other scenarios exchange-coupled interfaces at the twin plane between the misaligned variants of a grain remain counteracting the positive effect of a nonmagnetic grain boundary with respect to the switching field.

To quantify the M-H loop squareness we introduce the fullness factor, defined as $(MH)_{max}/(H_c M_r)$ [50]. Fig. 12 summarizes the absolute values of the switching fields, coercive fields, and the fullness factors for all scenarios. Whenever twinning defects are present, the loop squareness is lower compared to the corresponding scenario with same grain boundary properties but without twinning defect. The lowest values of the fullness factor occur for the fully exchange-decoupled grains with twin defects (scenarios c and h). In all scenarios the remanent magnetization is almost the same, 0.5 M_s, but they differ in coercivity. $(\mu_0 MH)_{max}$ is highest for scenario b) with 0.69 MJ/m^3 and lowest for scenario e) with 0.32 MJ/m^3 . But scenario b) also has the highest coercive field with 4.7 T and consequently a low fullness factor of 0.36. On

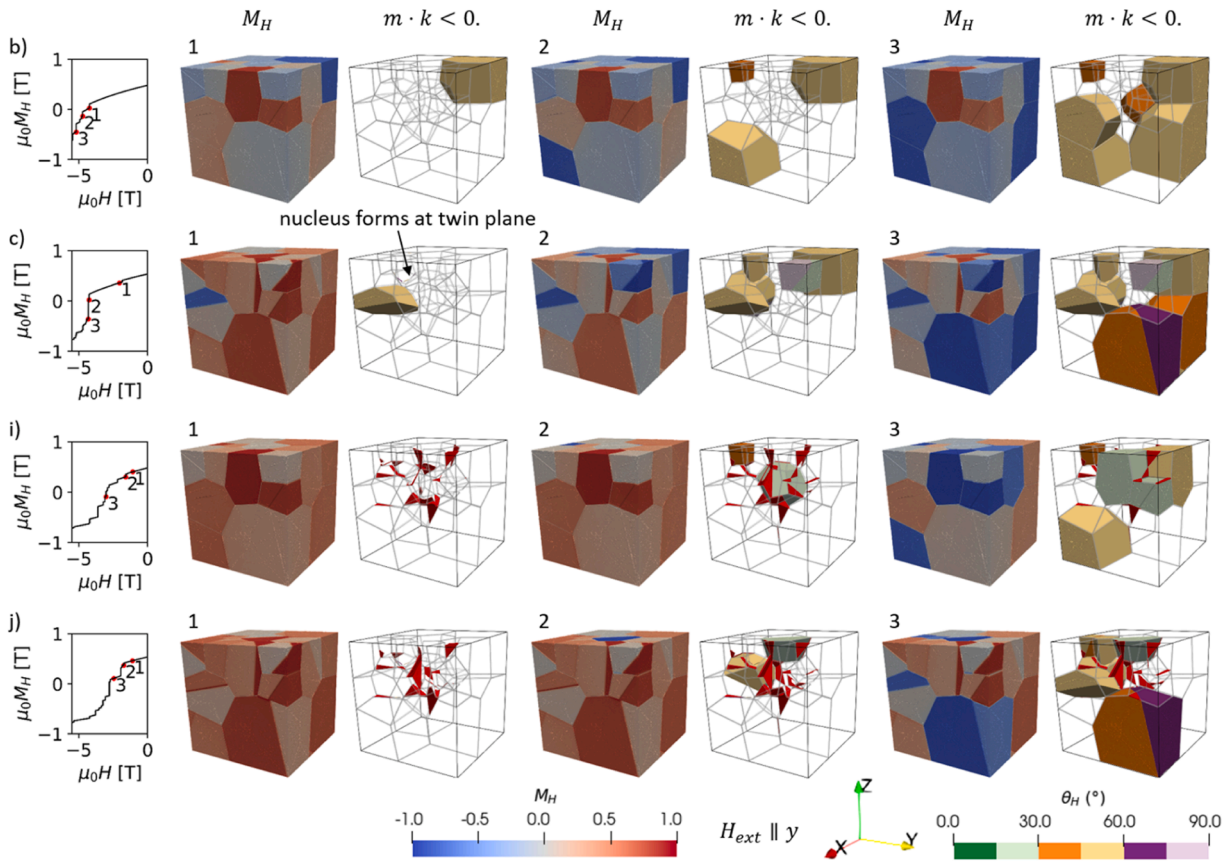

Fig. 13. Sketch of the magnetic reversal process in scenarios b), c), i) and j). For each scenario three magnetization states along the demagnetization curve are shown and marked in the plot on the left hand side in red. Each state shows the magnetization component parallel to the applied external field M_H and the parts of the magnet that reversed the magnetization identified by $m \cdot k < 0$, m - normalized magnetzation vector, k - easy axis vector. The colorscale for the reversed domain shows θ_H which is the misalignment of the easy axis with respect to the external field, colored in six 15°-wide categories. The external field was applied parallel to the y-axis.

the other hand, $\mu_0 H_c = 1.7$ T for scenario e) is the lowest coercive field of all considered scenarios, but the fullness factor is relatively high with 0.46. We also computed the maximum energy density product, $(BH)_{max}$, assuming a demagnetizing factor of 1/3 for cube-shaped magnets. The energy density produced was approximately 50 kJ/m^3 for all scenarios, which is close to the theoretical maximum for $(BH)_{max}$, $\mu_0 M_r^2/4 = 49.7$ kJ/m^3 . $(BH)_{max}$ was limited by the low remanence of the isotropic magnets.

Fig. 13 shows images of the magnetic reversal process for scenarios b), c), i) and j) and Fig. 14 shows images for scenarios a), d), e) and h). The images show the results of one of the 9 simulations per scenario. The reversed domain is identified according to $m \cdot k < 0$, where m is the normalized magnetization vector and k is the easy axis vector (see Fig. 1 in [46]).

In scenarios b) and c) a nonmagnetic grain boundary hinders the propagation of a reversed domain and grains initially reverse independently. Grains or twin variants with a misalignment angle with respect to the external field in the range of 30° to 60° switch first in accordance with the Stoner-Wohlfarth model. In scenario c) the initial nucleus within grains forms at twin planes (barely recognisable above the reversed domain in the first image due to the small size of the nucleus with respect to the model size) before one variant of the grain reverses. In scenarios i) and j) α-Fe is present and the initial nucleus forms there. Also better-aligned grains touching α-Fe may reverse earlier in accordance with theoretical results for the angular dependence of grains with defects presented in [51]. In scenario j) nucleation at twin planes is noticeable as well.

In scenarios a) and d) without grain boundary or only partial nonmagnetic grain boundary nucleation starts at coupled grain interfaces. In scenario e) additionally the nucleation at twin planes is observable. Strongly misaligned grains tend to reverse first followed by the expansion of the reversed domain. In scenario h) grains are separated by a nonmagnetic grain boundary and the initial nucleus again forms at the twin boundary. Most of grains showing twin defects reverse before any of the smaller regular grains. This agrees well with results presented in [42] that the switching field of isolated grains with twin defects in $ThMn_{12}$-type permanent magnets is below the lowest threshold of isolated Stoner-Wohlfarth grains.

4. Summary and conclusion

We have successfully prepared pure Cu-rich $Nd(Fe,Mo)_{12}$ based alloys by strip casting technique. Nitrogenation of the powders induce the increase of the Curie temperature and a huge increase of the anisotropy field. Detailed structural and microstructural characterizations of the $Nd(Fe,Mo)_{12}$ strip cast flakes reveal not only a non-uniform RE-Cu rich grain boundary distribution, but also the presence of twins, as already reported in the $Nd(Fe,Ti)_{12}$ [43] and $Sm(Fe,Ti)_{12}$ [42] systems. The misorientations angle across the twin boundary is approximately 58° and the twin boundary plane corresponds to a {0 1 1} family of the unit cell of $Nd(Fe,Mo)_{12}$. Down to the resolution of our TEM analysis, these twin boundaries are not segregated in elements, contrary to what has been revealed previously in $Sm(Fe,Ti)_{12}$ systems. As twin boundaries seems to appear in large grains (more than 400 nm), formation of twin boundaries can be attributed to the accumulation of internal stresses during solidification, where twin formation is favored over the formation of specific grain boundaries.

Micromagnetic simulations were carried out with a microstructure

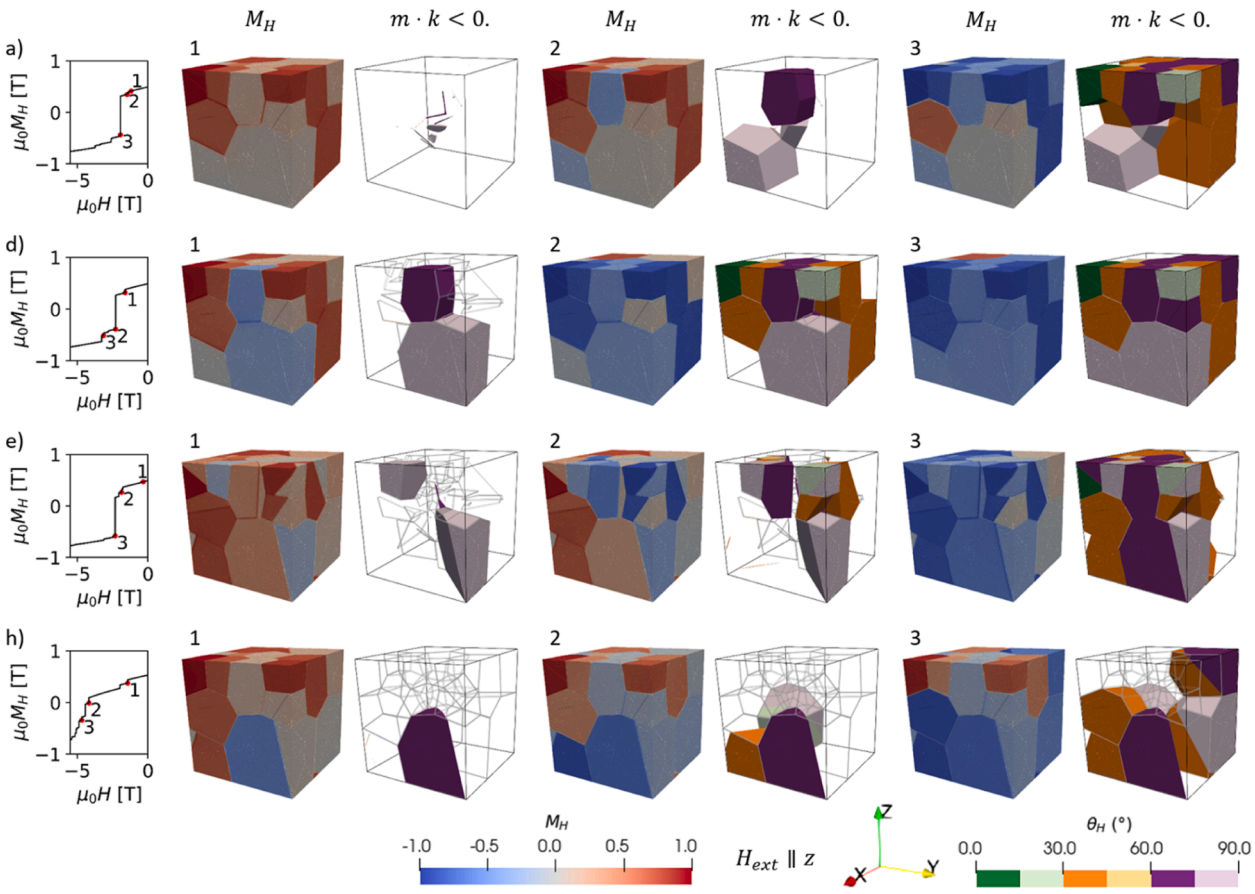

Fig. 14. Sketch of the magnetic reversal process in scenarios a), d), e) and h). The external field was applied parallel to the z-axis.

reproducing that of an ideal fully dense magnet, using the measured magnetic properties (H_a and M_s) of our nitrogenated powders and the microstructural observations of as cast flakes. The results show that non-magnetic grain boundaries are the key feature to maximize the coercivity and one of the factors to improve the switching field values. On the contrary, completely exchange coupled grains conduct to a huge drop in the coercivity and the switching field values. Partially exchange-coupled grains improve the coercivity, but do not represent the "best-case". This is the case highlighted by TEM analysis, and explains the low coercivity values measured on the powders, compared to the previously reported values [27].

The formation of twins does not significantly reduce the coercive field but for the same grain boundary configuration the switching fields are drastically reduced. The magnetization reversal starts at the twin plane interface between misoriented variants of the grains. The twin boundaries will act as nucleation sites due to partial domain walls forming. The low switching fields of grains with twinning defects will have a negative impact for high-performance permanent magnet applications. Formation of twin boundaries can be attributed to the accumulation of internal stresses during solidification, where twin formation is favored over the formation of specific grain boundaries. This is the case of large grains in our alloys, but still with sub-micrometric size. One pathway to overcome the formation of twins could be the grain size reduction to values below the limit of volume-to-surface energy ratio where there is no need to stress relief via twinning formation. This observation is supported by previous reported data, where twins were not evidenced in similar systems obtained by melt-spinning, that allow to reduce the grain size below 200 nm [16,27]. In addition, in the case of an isotropic configuration simulated here, the remanence is not affected by the presence of twinned grains, however to improve the energy density, the remanence should also be improved, in an anisotropic configuration. In this case, twining defect are harmful due to multiple easyaxes within a grain. It is therefore necessary to remove this cristallographic defects before the production of high performance Nd(Fe, Mo)$_{12}$ based permanent magnets.

In summary, we have demonstrated that the Cu-rich Nd(Fe,Mo)$_{12}$ system is a promising compound for permanent magnets, and identified areas for improvement to achieve the magnetic performance required for actual applications.

CRediT authorship contribution statement

Ryan Sedek: Investigation, Formal analysis, Conceptualization. **Patricia de Rango:** Validation, Supervision, Methodology, Funding acquisition, Conceptualization. **Gabriel Gomez Eslava:** Writing – original draft, Investigation, Formal analysis. **Thomas Schrefl:** Validation, Supervision, Methodology, Funding acquisition. **Sorana Luca:** Writing – review & editing, Writing – original draft, Supervision, Project administration, Funding acquisition, Formal analysis, Conceptualization. **Johann Fischbacher:** Writing – original draft, Methodology, Investigation, Conceptualization. **Camille Flament:** Writing – original draft, Methodology, Formal analysis.

Declaration of Competing Interest

The authors declare that they have no known competing financial interests or personal relationships that could have appeared to influence the work reported in this paper.

Acknowledgements

This work was supported by the Carnot Energies du Futur foundation

within the NAMASTE project. The financial support of the Austrian Federal Ministry of Labour and Economy, the National Foundation for Research, Technology and Development, Austria and the Christian Doppler Research Association, Austria is gratefully acknowledged.

Data availability

No data was used for the research described in the article.

References

[1] R. Gauß *et al.*, 'Rare Earth Magnets and Motors: A European Call for Action. A report by the Rare Earth Magnets and Motors Cluster of the European Raw Materials Alliance', Berlin 2021.

[2] J. Cui, et al., Current progress and future challenges in rare-earth-free permanent magnets, Acta Mater. 158 (Oct. 2018) 118–137, https://doi.org/10.1016/j.actamat.2018.07.049.

[3] K.H.J. Buschow, Permanent magnet materials based on tetragonal rare earth compounds of the type RFe12−xMx, J. Magn. Magn. Mater. 100 (1) (Nov. 1991) 79–89, https://doi.org/10.1016/0304-8853(91)90813-P.

[4] K. Hono, H. Sepehri-Amin, Prospect for HRE-free high coercivity Nd-Fe-B permanent magnets, Scr. Mater. 151 (Jul. 2018) 6–13, https://doi.org/10.1016/j.scriptamat.2018.03.012.

[5] K.P. Skokov, O. Gutfleisch, Heavy rare earth free, free rare earth and rare earth free magnets - Vision and reality, Scr. Mater. 154 (Sep. 2018) 289–294, https://doi.org/10.1016/j.scriptamat.2018.01.032.

[6] Y. Hirayama, Y.K. Takahashi, S. Hirosawa, K. Hono, NdFe12Nx hard-magnetic compound with high magnetization and anisotropy field', Scr. Mater. 95 (Jan. 2015) 70–72, https://doi.org/10.1016/j.scriptamat.2014.10.016.

[7] T. Sato, T. Ohsuna, M. Yano, A. Kato, Y. Kaneko, Permanent magnetic properties of NdFe12Nx sputtered films epitaxially grown on V buffer layer, J. Appl. Phys. 122 (5) (Aug. 2017) 053903, https://doi.org/10.1063/1.4991750.

[8] M. Endoh, K. Nakamura, H. Mikami, Nd(Fe,Mo)/sub 12/N/sub x/ compounds and magnets, IEEE Trans. Magn. 28 (5) (Sep. 1992) 2560–2562, https://doi.org/10.1109/20.179556.

[9] Y. Yang, J. Yang, J. Han, C. Wang, S. Liu, H. Du, Research and development of interstitial compounds, IEEE Trans. Magn. 51 (11) (Nov. 2015) 1–6, https://doi.org/10.1109/TMAG.2015.2442244.

[10] J. Yang, et al., Magnetic properties and magnetic domain structures of NdFe10.5Mo1.5 and NdFe10.5Mo1.5Nx, Appl. Phys. Lett. 71 (22) (Dec. 1997) 3290–3292, https://doi.org/10.1063/1.120315.

[11] J.S. Zhang, et al., Microstructure and extrinsic magnetic properties of anisotropic Sm(Fe,Ti,V)12-based sintered magnets, Acta Mater. 238 (Oct. 2022) 118228, https://doi.org/10.1016/j.actamat.2022.118228.

[12] J.S. Zhang, X. Tang, H. Sepehri-Amin, A.K. Srinithi, T. Ohkubo, K. Hono, Origin of coercivity in an anisotropic Sm(Fe,Ti,V)12-based sintered magnet, Acta Mater. 217 (Sep. 2021) 117161, https://doi.org/10.1016/j.actamat.2021.117161.

[13] A.M. Gabay, R. Cabassi, S. Fabbrici, F. Albertini, G.C. Hadjipanayis, Structure and permanent magnet properties of Zr1-xRxFe10Si2 alloys with R = Y, La, Ce, Pr and Sm, J. Alloy. Compd. 683 (Oct. 2016) 271–275, https://doi.org/10.1016/j.jallcom.2016.05.092.

[14] D. Niarchos, et al., Intrinsic magnetic properties of (Nd1−xSmx)Fe11Ti, J. Alloy. Compd. 864 (May 2021) 158097, https://doi.org/10.1016/j.jallcom.2020.158097.

[15] J.M. Barandiaran, et al., Nitrogenation and sintering of (Nd-Zr)Fe10Si2 tetragonal compounds for permanent magnets applications, J. Alloy. Compd. 784 (May 2019) 996–1002, https://doi.org/10.1016/j.jallcom.2019.01.044.

[16] A. Aubert, et al., Structural and magnetic properties of Nd-Fe-Mo-(N) melt-spun ribbons with ThMn12 structure, Acta Mater. 195 (Aug. 2020) 519–526, https://doi.org/10.1016/j.actamat.2020.05.045.

[17] A.M. Schönhöbel, et al., Intrinsic magnetic properties of SmFe12−xVx alloys with reduced V-concentration', J. Alloy. Compd. 786 (2019) 969–974, https://doi.org/10.1016/j.jallcom.2019.01.332.

[18] M. Bacmann, et al., Exchange interactions and magneto-crystalline anisotropy in RFe12−xMx and parent interstitial compounds', J. Alloy. Compd. 383 (1) (Nov. 2004) 166–172, https://doi.org/10.1016/j.jallcom.2004.04.083.

[19] J. Yang, Y. Yang, Magnetic properties and interstitial atom effects in the R (Fe, M) 12 compounds', Handb. Adv. Magn. Mater. (2006) 1414–1451.

[20] A.K. Srinithi, X. Tang, H. Sepehri-Amin, J. Zhang, T. Ohkubo, K. Hono, High-coercivity SmFe12-based anisotropic sintered magnets by Cu addition, Acta Mater. 256 (Sep. 2023) 119111, https://doi.org/10.1016/j.actamat.2023.119111.

[21] C. Christides, A. Kostikas, A. Simopoulos, D. Niarchos, G. Zouganelis, A study of spin reorientation in NdFe12-xVx by Mössbauer and magnetization measurements, J. Magn. Magn. Mater. 86 (2) (May 1990) 367–376, https://doi.org/10.1016/0304-8853(90)90145-G.

[22] T. Fukazawa, H. Akai, Y. Harashima, T. Miyake, First-principles study of intersite magnetic couplings in NdFe12 and NdFe12X (X = B, C, N, O, F), J. Appl. Phys. 122 (5) (Aug. 2017) 053901, https://doi.org/10.1063/1.4996989.

[23] L. Zhongyi, J. Zhanpeng, A study of the Nd–Fe–Mo system at 600°C, J. Alloy. Compd. 252 (1) (May 1997) 230–233, https://doi.org/10.1016/S0925-8388(96)02586-8.

[24] E. Semenova, Iron – Molybdenum – Neodymium, Refract. Met. Syst. (2010) 257–269.

[25] X. Kong, et al., Nitrogenation effect of Nd(Fe,Mo)12 alloys prepared by strip casting technique, J. Alloy. Compd. 506 (2) (Sep. 2010) 858–861, https://doi.org/10.1016/j.jallcom.2010.07.095.

[26] M.-R. Jian, T.-S. Chin, J.-L. Tsai, H.-W. Zhang, B.-G. Shen, Structure and magnetic properties of textured Nd(Fe,Ti)12Nx films, J. Magn. Magn. Mater. 209 (1) (Feb. 2000) 205–207, https://doi.org/10.1016/S0304-8853(99)00688-5.

[27] A. Aubert, et al., Denitrogenation process in ${\mathrm{ThMn}}_{12}$ nitride by in situ neutron powder diffraction, Phys. Rev. Mater. 5 (1) (Jan. 2021) 014415, https://doi.org/10.1103/PhysRevMaterials.5.014415.

[28] E.F. Rauch, M. Véron, Automated crystal orientation and phase mapping in TEM, Mater. Charact. 98 (Dec. 2014) 1–9, https://doi.org/10.1016/j.matchar.2014.08.010.

[29] D. Kinderlehrer, L. Ma, The hysteretic event in the computation of magnetization, J. Nonlinear Sci. 7 (2) (Apr. 1997) 101–128, https://doi.org/10.1007/BF02677975.

[30] L. Exl, J. Fischbacher, A. Kovacs, H. Oezelt, M. Gusenbauer, T. Schrefl, Preconditioned nonlinear conjugate gradient method for micromagnetic energy minimization, Comput. Phys. Commun. 235 (Feb. 2019) 179–186, https://doi.org/10.1016/j.cpc.2018.09.004.

[31] Q. Chen, A. Konrad, A review of finite element open boundary techniques for static and quasi-static electromagnetic field problems, IEEE Trans. Magn. 33 (1) (Jan. 1997) 663–676, https://doi.org/10.1109/20.560095.

[32] D.E. Demidov, D.V. Shevchenko, Modification of algebraic multigrid for effective GPGPU-based solution of nonstationary hydrodynamics problems, J. Comput. Sci. 3 (6) (Nov. 2012) 460–462, https://doi.org/10.1016/j.jocs.2012.08.008.

[33] R. Quey, P.R. Dawson, F. Barbe, Large-scale 3D random polycrystals for the finite element method: Generation, meshing and remeshing, Comput. Methods Appl. Mech. Eng. 200 (17) (Apr. 2011) 1729–1745, https://doi.org/10.1016/j.cma.2011.01.002.

[34] R. Quey, L. Renversade, Optimal polyhedral description of 3D polycrystals: method and application to statistical and synchrotron X-ray diffraction data, Comput. Methods Appl. Mech. Eng. 330 (Mar. 2018) 308–333, https://doi.org/10.1016/j.cma.2017.10.029.

[35] Salome, '⟨https://www.salome-platform.org/⟩, accessed 17th April 2024'.

[36] Meshgems, 'MeshGems used within the SMESH module of Salome, ⟨https://www.spatial.com/products/3d-precise-mesh⟩, accessed 17th April 2024.'

[37] E.W. Weisstein, '"Sphere Point Picking." From MathWorld–A Wolfram Web Resource. ⟨https://mathworld.wolfram.com/SpherePointPicking.html⟩'.

[38] R. Sedek, S. Luca, P. de Rango, Nitrogenation of Nd(Fe,Mo)12 powders for sintered magnets, J. Alloy. Compd. 1006 (Nov. 2024) 176063, https://doi.org/10.1016/j.jallcom.2024.176063.

[39] P. Qi, Z. Xiao-dong, Z. Ming-hou, Y. Ying-chang, Magnetic properties of new series *R* -Mo-Fe nitrides with the ThMn $_{12}$ -type structure at a lower Mo content, Acta Phys. Sin. Overseas Ed. 3 (6) (Jun. 1994) 460–469, https://doi.org/10.1088/1004-423X/3/6/009.

[40] X.F. Liao, et al., Grain boundary engineering in Nd-based ThMn12 magnets and their nitrides: a comprehensive study of challenges and limitations, J. Alloy. Compd. 950 (Jul. 2023) 169933, https://doi.org/10.1016/j.jallcom.2023.169933.

[41] W. Mo, L. Zhang, Q. Liu, A. Shan, J. Wu, M. Komuro, Dependence of the crystal structure of the Nd-rich phase on oxygen content in an Nd–Fe–B sintered magnet, Scr. Mater. 59 (2) (Jul. 2008) 179–182, https://doi.org/10.1016/j.scriptamat.2008.03.004.

[42] S. Ener, et al., Twins – A weak link in the magnetic hardening of ThMn12-type permanent magnets, Acta Mater. 214 (Aug. 2021) 116968, https://doi.org/10.1016/j.actamat.2021.116968.

[43] F. Maccari, et al., Rapid solidification of Nd1+XFe11Ti compounds: phase formation and magnetic properties, Acta Mater. 180 (Nov. 2019) 15–23, https://doi.org/10.1016/j.actamat.2019.08.057.

[44] A. Kovacs, et al., Physics-informed machine learning combining experiment and simulation for the design of neodymium-iron-boron permanent magnets with reduced critical-elements content, Front. Mater. 9 (Jan. 2023), https://doi.org/10.3389/fmats.2022.1094055.

[45] E.C. Stoner and E.P. Wohlfarth, 'A mechanism of magnetic hysteresis in heterogeneous alloys | Philosophical Transactions of the Royal Society of London. Series A, Mathematical and Physical Sciences'. Accessed: May 02, 2024. [Online]. Available: ⟨https://royalsocietypublishing.org/doi/10.1098/rsta.1948.0007⟩.

[46] G. Martinek, H. Kronmüller, Influence of grain orientation of the coercive field in Fe-Nd-B permanent magnets, J. Magn. Magn. Mater. (May 1990) 177–183.

[47] T. Schrefl, H.F. Schmidts, J. Fidler, H. Kronmüller, The role of exchange and dipolar coupling at grain boundaries in hard magnetic materials, J. Magn. Magn. Mater. (Jun. 1993) 251–261.

[48] E.F. Kneller, The exchange-spring magnet: a new material principle for permanent magnets, ', *IEEE Trans. Magn.* (1991).

[49] P. Zhao, Nanoscale chemical segregation to twin interfaces in τ-MnAl-C and resulting effects on the magnetic properties', J. Mater. Sci. Technol. 134 (Jan. 2023) 22–32.

[50] J.M. Niedra, 'NASA Contractor Report No. 194440', Mar. 1994.

[51] G. Rieger, M. Seeger, H. Kronmüller, 'Microstructural parameters in high-remanent sintered NdFeB magnets', Phys. Status Solidi A 171 (2) (1999) 583–596, https://doi.org/10.1002/(SICI)1521-396X(199902)171:2< 583::AID-PSSA583> 3.0.CO;2-C.